

# Impact of environmental oxygen on nanoparticle formation and agglomeration in aluminum laser ablation plumes

Elizabeth J. Kautz,<sup>1,2</sup> Alla Zelenyuk,<sup>1</sup> Bharat Gwalani,<sup>1,3</sup> Matthew J. Olszta,<sup>1</sup> Mark C. Phillips,<sup>4</sup> Manuel J. Manard,<sup>5</sup> Clare W. Kimblin,<sup>5</sup> and Sivanandan S. Harilal<sup>1</sup>

<sup>1</sup>*Pacific Northwest National Laboratory, Richland, Washington 99352, USA*

<sup>2</sup>*Nuclear Engineering Department, North Carolina State University, Raleigh, North Carolina 27695, USA*

<sup>3</sup>*Materials Science and Engineering Department, North Carolina State University, Raleigh, North Carolina 27695, USA*

<sup>4</sup>*James C. Wyant College of Optical Sciences, University of Arizona, Tucson, Arizona 85721, USA*

<sup>5</sup>*Special Technologies Laboratory, Santa Barbara, California 93111, USA*

(\*Electronic mail: hari@pnnl.gov)

(\*Electronic mail: ekautz@ncsu.edu)

(Dated: 26 September 2023)

The role of ambient oxygen gas ( $O_2$ ) on molecular and nanoparticle formation and agglomeration was studied in laser ablation plumes. As a lab-scale surrogate to a high explosion detonation event, nanosecond laser ablation of an aluminum alloy (AA6061) target was performed in atmospheric pressure conditions. Optical emission spectroscopy and two mass spectrometry techniques were used to monitor the early to late stages of plasma generation to track the evolution of atoms, molecules, clusters, nanoparticles, and agglomerates. The experiments were performed under atmospheric pressure air, atmospheric pressure nitrogen, and 20 and 5 %  $O_2$  (balance  $N_2$ ), the latter specifically with in-situ mass spectrometry. Electron microscopy was performed ex-situ to identify crystal structure and elemental distributions in individual nanoparticles. We find that the presence of  $\approx 20$  %  $O_2$  leads to strong AIO emission, whereas in a flowing  $N_2$  environment (with trace  $O_2$ ), AlN and strong, unreacted Al emissions are present. In-situ mass spectrometry reveals that as  $O_2$  availability increases, Al oxide cluster size increases. Nanoparticle agglomerates formed in air are found to be larger than those formed under  $N_2$  gas. High-resolution transmission electron microscopy demonstrates that  $Al_2O_3$  and AlN nanoparticle agglomerates are formed in both environments; indicating that the presence of trace  $O_2$  can lead to  $Al_2O_3$  nanoparticle formation. The present results highlight that the availability of  $O_2$  in the ambient gas significantly impacts spectral signatures, cluster size, and nanoparticle agglomeration behavior. These results are relevant to understanding debris formation in an explosion event, and interpreting data from forensic investigations.

Keywords: nanoparticle, laser-produced plasma, plasma chemistry, agglomeration, high explosion

## I. INTRODUCTION

Aluminum (Al) is a lightweight metal that has been widely used in aerospace, automobile, and defense applications owing to its high strength-to-weight ratio, and durability in harsh environments.<sup>1</sup> For example, select weapons components are fabricated from pure Al or Al alloys that are able to withstand wear, damage, corrosion, and undergo combustion in the presence of oxygen ( $O_2$ ). Al is also used as a fuel in solid energetic materials to generate heat, gas, and thrust for propulsion, pyrotechnic, and microelectromechanical systems.<sup>2,3</sup> Given the widespread use of Al-based materials as components in weapons and explosives design (e.g., case materials in high-explosive charges), debris generated from combustion or a high explosion (HE) detonation event is likely to contain Al-bearing particulate material. However, the fundamental mechanisms and pathways for debris formation in such HE events are not well-understood, in part due to the experimental complexities in tracking numerous phenomena occurring over a wide range of time and length scales.

There is growing interest in using laser-produced plasmas (LPPs) or laser ablation plumes as a lab-scale testbed for studying the physical and chemical processes that occur in

HE events, given comparable, relevant temperatures can be achieved.<sup>4-12</sup> Although large-scale detonation tests have been performed and yield valuable data,<sup>13-15</sup> there are several associated challenges, including the high cost and time-consuming nature of these tests. It can also be difficult to study detonations using spectroscopic tools due to strong background radiation, and the need to use long gate widths to account for reduced signal at standoff distances, precluding high time-resolution measurements. Further, the systematic production and collection of debris formed in these large-scale tests present yet another challenge in reconstructing nanoparticle (NP) formation pathways. Small-scale HE tests have also explored emission and absorption signatures of uranium, case materials (e.g., Al alloys, steels, Mg alloys), and high explosives (e.g., TNT -  $C_7H_5N_3O_6$ , PETN -  $C_5H_8N_4O_{12}$ ).<sup>16-18</sup> Instead, LPPs offer a microscopic, lab-scale alternative that can provide data to build predictive capabilities for modeling NP formation and agglomeration in an HE event. LPPs can also help inform forensic investigations involving NP agglomerate and debris characterization.<sup>19</sup>

Experiments using LPPs as a surrogate for HE events involve laser ablation (LA) of a target material of interest to generate a plasma. After plasma generation, collisions between

plasma species and the ambient media lead to plume confinement, and thermo- and plasma-chemical reactions. The thermo- and plasma-chemical reactions possible in an LPP are defined by plasma initial conditions (i.e., temperature, density), and the nature and pressure of the ambient gas. In an oxygen-containing environment (e.g., air), molecules such as metal oxides can be formed. The temperatures favorable for metal oxide formation (e.g., AlO, FeO, TaO, UO, etc.) depend on the system and typically occur at temperatures less than 8000 K.<sup>4,20</sup> Metal oxides are formed through several possible reaction channels. For example, in the Al-O system, there are numerous reaction channels that can lead to Al oxide molecular formation, such as:  $\text{Al} + \text{O}_2 \rightleftharpoons \text{AlO} + \text{O}$ .<sup>9,20,21</sup> These metal oxides can then act as precursors to higher oxides, clusters, and eventually nucleation sites for NPs that form NP agglomerates.

The aggregation of NPs in a gaseous environment is controlled by several factors, including interfacial chemical reactions and particle transport mechanisms. The tendency for NPs to agglomerate impacts their mobility and interaction with the environment. The dynamics and mechanisms of NP formation and agglomeration have been extensively studied during and after combustion.<sup>22,23</sup> Some of the proposed phenomena related to NP and agglomerate formation include condensation, nucleation, and coagulation.<sup>22</sup> The process of homogeneous nucleation depends strongly on factors such as local cooling rates, constituents present in the gas phase, and degree of saturation or supersaturation. A study on combustion products in diesel fuels found that Fe-doping above a given Fe:C ratio (0.013), led to the formation of distinctly different NP morphologies, size distributions, and compositions; with increasing Fe content in the fuel, the size of primary NPs and agglomerates increased, and both metallic Fe and Fe oxide NPs were observed.<sup>22</sup> In our prior work on LA of a multi-component target (10% Al, 30% Ti, 20% Zr, 20% Nb, 15% Ta, 5% V - in at. %), we found that at high cooling rates in atmospheric pressure air, amorphous NPs with diameters less than 10 nm consisting of all elements and oxygen were formed.<sup>6</sup> In addition, crystalline Ti oxide NPs were formed. The amorphous NPs were hypothesized to form via homogeneous nucleation from a supersaturated vapor phase, whereas the larger crystalline NPs were likely formed where plasma temperatures were cooler, via heterogeneous nucleation. These NPs were found to form fractal agglomerates.<sup>6</sup> Hence, numerous parameters including plasma and gas-phase physical conditions, the species present and their concentrations all strongly impact NP structure, composition, and size, and these in turn impact NP agglomeration behavior.

While numerous experimental and modeling studies have explored NP formation routes via pulsed LA in aqueous and low-pressure gaseous environments,<sup>24–27</sup> NP formation mechanisms are still not well-known for reactive, gaseous environments such as atmospheric pressure air relevant to HE events. Previous studies have also primarily focused on limited time scales (either early time formation, studied using emission spectroscopy, or later times/after the formation of NPs, studied via microscopy/surface characterization).<sup>27–29</sup> Hence an improved understanding of NP formation mechanisms in at-

mospheric pressure gaseous environments is needed. The aim of this work is to investigate the role of O<sub>2</sub> in the environment on NP formation and agglomeration by following the evolution of species (atomic through agglomerate) produced by laser ablation of an Al alloy substrate. Due to its relevance to particulate formation during HE events, laser ablation was performed in air at atmospheric pressure, and in nitrogen with minimal oxygen content. Supporting in-situ mass spectrometry studies performed in 5 and 20% O<sub>2</sub> (balance N<sub>2</sub>) are also presented.

## II. EXPERIMENTAL METHODS

LA was performed using 1064 nm, 6 ns full-width half maximum (FWHM) pulses from an Nd:YAG laser on an Al alloy (AA6061) target. The composition of the AA6061 target is defined by ASTM as follows (all in wt. %): 0.40-0.8 Si, 0.7 Fe, 0.15-0.4 Cu, 0.15 Mn, 0.8-1.2 Mg, 0.04 - 0.35 Cr, 0.25 Zn, 0.15 Ti, remainder Al.<sup>30</sup> The laser fluence at the target was  $\approx 12 \text{ J/cm}^2$ . These laser parameters were selected to generate a plasma that undergoes plume chemistry similar to a detonation event.<sup>4</sup> A schematic describing the experimental workflow is given in Figure 1. The target was placed in a vacuum chamber for ambient gas control, which was mounted onto an x-y translator to move the target during LA to prevent drilling. Prior to the collection of spectral data, the native oxide on the AA6061 target was removed via LA. Multiple optical windows and ports for laser entrance, light collection, and electronics were included in the chamber design. A pressure gauge, vacuum pump, and gas lines were also attached to the chamber to control the nature and pressure of the ambient medium. For OES, and particles generated for particulate size distribution and single particle mass spectrometry, laser ablation was carried out at atmosphere pressure ( $\approx 750$  Torr) where the environment was varied from flowing dry air (with  $\approx 20 \%$  O<sub>2</sub>) to N<sub>2</sub> (99.99 % purity). Multiple diagnostic tools were used to track the real-time progression of atoms-diatoms- larger molecules-aerosols-particulates, details of which are given below. The properties of the particulates generated were characterized using ex-situ tools such as scanning transmission electron microscope (STEM) and energy dispersive spectroscopy (EDS).

### A. Optical emission spectroscopy

Optical emission spectroscopy (OES) is used for tracking the atoms and smaller molecules (e.g. diatoms) in the ablation plume as well as for the physical characterization of the plasma. For performing OES, the UV-VIS emission from the plasma is collected in a spatially integrated manner and transported to a 0.75 m spectrograph (SpectraPro HRS-750, Princeton Instruments) equipped with an intensified CCD (ICCD, PIMAX4, Princeton Instruments) using an optical fiber. Broad spectral measurements were analyzed using the 300 grooves/mm grating ( $\approx 0.1 \text{ nm}$  resolution), while the 2400 grooves/mm grating ( $\approx 0.02 \text{ nm}$ ) was used for col-

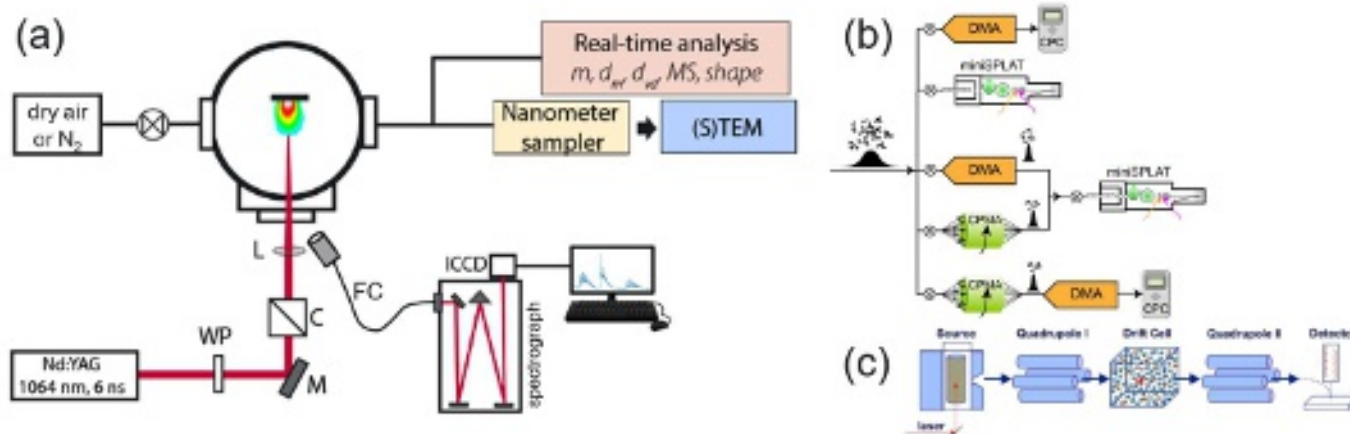


FIG. 1. (a) Experimental workflow for LPP and NP generation, and characterization, including ns LA using a Nd:YAG laser, real-time, (S)TEM analysis, and QCQ mass spectrometry analyses. Parameters obtained in real-time analysis (detailed in sub-figure b) include:  $m$  (mass),  $d_m$  (mobility diameter),  $d_{va}$  (vacuum aerodynamic diameter), MS (mass spectrum), and shape. Acronyms used in the schematic are defined as follows: WP (wave plate), M (mirror), C (cube polarizer), L (lens), FC (fiber cable), ICCD (intensified charged coupled device), STEM (Scanning Transmission Electron Microscopy). (b) Schematic of different pathways for real-time analysis, including the following components: DMA (differential mobility analyzer), CPC (condensation particle counter), miniSPLAT (a single particle mass spectrometer), and CPMA (centrifugal particle mass analyzer). (c) Schematic of the and QCQ (Quadrupole-Cell-Quadrupole) mass spectrometry analysis method which was performed at 5 and 20 % O<sub>2</sub>.

lecting high-resolution spectra for Stark broadening and temperature measurements.

### B. Quadrupole-Cell-Quadrupole mass spectrometry

A custom-built quadrupole-cell-quadrupole (QCQ) mass spectrometer was used to directly study larger molecules generated via laser ablation. Details of the system are given in elsewhere.<sup>31</sup> The instrument is based on the design of Kemper and Bowers.<sup>32,33</sup> Briefly, the QCQ system consists of a high-pressure reaction cell that is embedded between two quadrupole mass analyzers (Extrel Tri-filter Quadrupole Mass Filters). Both quadrupoles have a mass range of  $m/z = 4 - 4000$ . Aluminum oxide clusters are generated by pulsed laser vaporization of a translating/rotating AA6061 rod in a high-pressure bath gas consisting of N<sub>2</sub> seeded with O<sub>2</sub> at varying concentrations (5 and 20%). Ions exiting the source can either be mass selected by the first quadrupole mass filter, or all ions can be allowed to pass through this region of the instrument (as was done here). The ions are then injected into the reaction cell. The reaction cell is a Cu block that is 4 cm in length, with an entrance and exit orifice measuring 0.5 mm in diameter. For the purposes of this experiment, the cell was filled with an inert gas (He) so that all ions generated in the source could drift through the cell unaltered. Typical gas pressures in the cell range from 1.5 to 4 Torr, rather than 750 Torr. Ions are drawn through the cell under the influence of a weak electric field which does not significantly perturb the thermal energy of the ions. Upon exiting the cell, ions are mass analyzed by a second quadrupole mass filter and detected using a conversion dynode and Channeltron electron multiplier.

### C. Particulate size distribution and single particle mass spectrometry

Mobility diameter ( $d_m$ ) size distributions of 750 Torr LA-generated particles were obtained using a Scanning Mobility Particle Sizer (SMPS), comprised of a differential mobility analyzer (DMA, Model 3081, TSI Inc.) and a condensation particle counter (CPC, Model 3786, TSI Inc). In order to minimize coagulation of particles during transport and analysis, the SMPS was located in close vicinity to the LA cell; this close proximity limited particle transport time to  $\approx 1-3$  s. The generated particulates were flushed out from the chamber by flowing air or N<sub>2</sub> (with trace oxygen) at 5 lpm (liters per minute). Mass spectra and vacuum aerodynamic diameters ( $d_{va}$ ) of individual LA-generated particles were measured with miniSPLAT, a single-particle mass spectrometer.<sup>6,34,35</sup> For the miniSPLAT measurements, LA-generated particles were first introduced into a 100 L Teflon sampling chamber prefilled with dry N<sub>2</sub>, where they were diluted by a factor of  $\approx 10$  to minimize particle coagulation. miniSPLAT was also used to characterize the size and mass-selected particles classified by a DMA and a centrifugal particle mass analyzer (CPMA, Cambustion), respectively. Similarly, SMPS was used to measure  $d_m$  size distributions of mass-selected particles. Combined, these measurements yield information on the fractal dimension of NP agglomerates and their effective densities. For the materials with known densities, these measurements also yield the average diameter of primary NP, number of primary NPs, void fraction, and dynamic shape factors as a function of particle mass or size.<sup>35</sup>

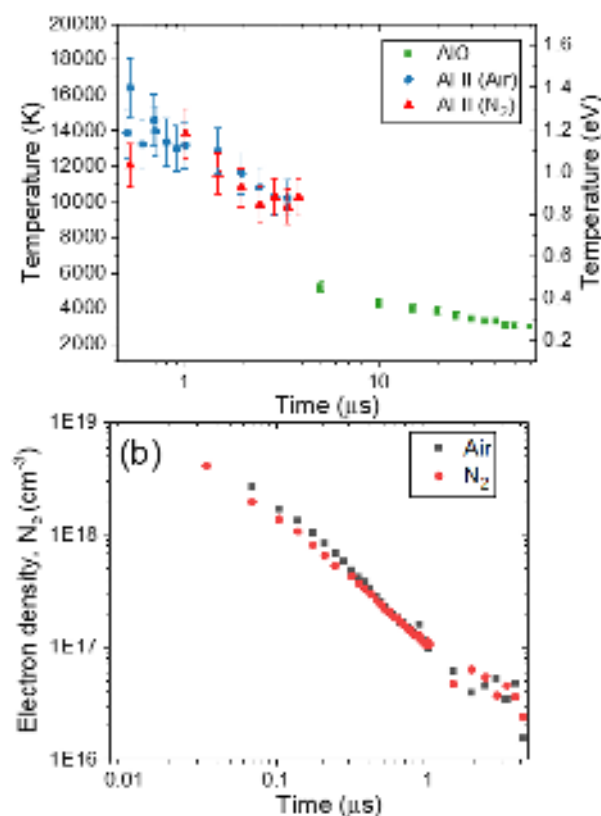


FIG. 2. Time-resolved physical conditions of LPPs in air and N<sub>2</sub>: (a) excitation temperature (K), and (b) electron density (cm<sup>-3</sup>). Gate delay is given as the x-axis (Time in  $\mu\text{s}$ ), and gate width varied based on gate delay. For Al II temperature and density measurements, a progressive gate width of 10 % of the gate delay value was used. For AIO temperature measurements, a gate width of 5  $\mu\text{s}$  was used for gate delays of 5–40  $\mu\text{s}$ , and a 20  $\mu\text{s}$  gate width was used for delays of 50  $\mu\text{s}$  and greater. The timing jitter for the laser and detector were less than 1 ns.

#### D. Scanning/Transmission Electron Microscopy (STEM)

NPs and NP agglomerates generated during 750 Torr LA were characterized via TEM by depositing them on Lacey Formvar/Carbon mesh gold grids using a Nanometer Aerosol Sampler (Model 3089, TSI Inc) for 5 minutes at a sampling flow rate of 1 lpm. Analysis was performed using an aberration (Cs) corrected JEOL ARM200CF transmission electron microscope operated at 200 keV, equipped with a JEOL Centurio energy dispersive spectrometer (EDS) with a collection angle of 0.9 sr. Analysis was performed in scanning mode including annular darkfield (ADF). Digital imaging data collection was achieved using Gatan Microscopy Suite (GMS version 3) and EDS data collection and analysis was performed using Thermo Fisher Pathfinder software (Version 1.2.)

### III. RESULTS

The physical conditions (i.e., excitation temperature and electron density) of laser ablation Al plumes at early times of its evolution were determined based on Al II and AIO emission spectral features, with results reported in Figure 2. The excitation temperature ( $T_e$ ) was estimated via the Boltzmann method,<sup>36</sup> using Al II transitions at 263.15 nm, 266.92 nm, and 281.62 nm for times  $\leq 5 \mu\text{s}$ . The temperature, in air ambient, at later times ( $\geq 5 \mu\text{s}$ ) was estimated from the (0,1) AIO band (with a strong bandhead at  $\approx 508 \text{ nm}$ ) using the PGO-PHER simulation tool.<sup>36–38</sup> Electron density ( $N_e$ ) was determined from the Stark broadening of the Al II transition at 281.62 nm. Spectroscopic constants of the selected transitions are readily available in the literature,<sup>39</sup> and the impact parameter of Al II transition was obtained from Konjevic *et al.*<sup>40</sup> The time evolution of  $T_e$  and  $N_e$  was carried out in a spatially integrated manner and hence it represents average conditions in an inhomogeneous plume.

As Figure 2(a) shows, the Al II excitation temperatures are initially similar for both air and N<sub>2</sub> environments; from  $\approx 500 \text{ ns} - 5 \mu\text{s}$  temperatures drop from  $\approx 16000$  to 12000 K. At later times in air, from  $\approx 5 - 60 \mu\text{s}$ , the AIO molecular temperature was measured to range between  $\approx 6000 \text{ K} - 3000 \text{ K}$ . Temperatures at later times in N<sub>2</sub> could not reliably be determined, owing to a lack of Al II or near absence of AIO emission. Electron densities (Figure 2(b)) are also similar for plasmas at early times (up to  $\approx 4 \mu\text{s}$ ) in both environments. The similarities in both excitation temperature and electron densities at early times ( $\leq 3 \mu\text{s}$ ) in air and N<sub>2</sub> indicate that initial plasma physical conditions are not significantly impacted by the presence of oxygen in the environment, particularly in the relatively high background pressure of 750 Torr.

Broad emission spectral features were collected in air and N<sub>2</sub> environments, with results reported in Figure 3(a) and (b), respectively, in order to understand the impact of environmental oxygen on spectral signatures of LPPs. Spectra were collected in a spatially integrated manner at a gate delay/width of 50  $\mu\text{s}/50 \mu\text{s}$  when molecular emission is expected to be prominent. In the air ambient, atomic (Al I) and molecular (AIO green system,  $B^2\Sigma^+ - X^2\Sigma^+$ ) emission signatures are the strongest. In N<sub>2</sub>, the spectrum is dominated by strong Al I lines along with weak AlN band at 508 nm.<sup>41,42</sup>

As time evolves, the smaller molecules in the plume (e.g., diatoms) may be consumed in the formation of larger molecules (i.e., AlO<sub>2</sub>, Al<sub>2</sub>O<sub>3</sub>, Al<sub>x</sub>O<sub>y</sub>),<sup>43</sup> or form clusters that act as precursors for NPs. However, optical emission spectroscopy is not a viable tool to monitor the presence of larger molecules in the plume. To investigate later times in plasma evolution when higher oxides and clusters can form, the QCC mass spectrometer was used to characterize aluminum oxide cluster formation with varying oxygen partial pressures. Here, LA of an AA6061 target in an ambient environment with 5 and 20 % O<sub>2</sub> (where the remaining gas was kept as N<sub>2</sub>) was conducted and Al oxide cluster ions were monitored from 100 - 500  $\mu\text{s}$ . An example mass spectrum is reported in Figure 4(a), with ratios of O:Al in Al<sub>m</sub>O<sub>n</sub> clusters given for 5 and 20 % O<sub>2</sub> in Figure 4(b). From mass spectrometry results, we find that

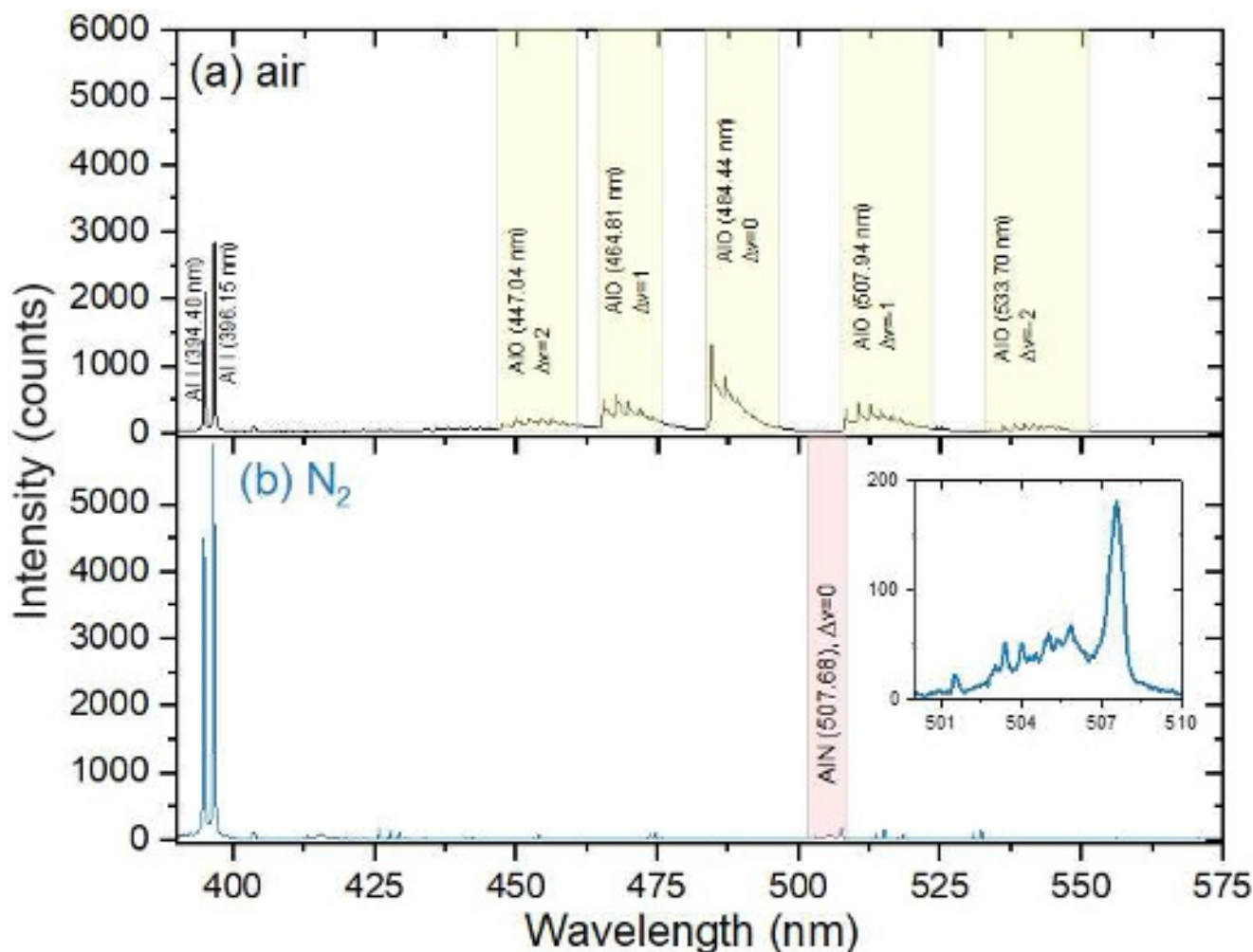


FIG. 3. Broad emission spectral features for plasmas produced from an AA6061 target material in 750 Torr (a) air, and (b) N<sub>2</sub>. The figure inset in (b) shows the AlN band labeled in the broad spectra. Spectra were collected in a spatially-integrated manner at a gate delay/width of 50  $\mu$ s/50  $\mu$ s using a 300 grooves/mm grating.

as the percentage of O<sub>2</sub> in the ambient environment increases, the ratio of O:Al stays approximately constant at 1.5 (i.e., 3 O atoms for every 2 Al atoms), but the number of Al and O atoms increases. This result highlights that with increasing O<sub>2</sub> availability, Al oxide cluster size increases, and the ratio of O:Al is consistent with an Al<sub>2</sub>O<sub>3</sub> stoichiometry.

The size distributions of NPs, and their agglomerates formed in flowing air and N<sub>2</sub> (with trace oxygen) environments are monitored using SMPS, with results reported in Figure 5. Here, the number concentration of particulates (i.e., NP agglomerates) is plotted as a function of mobility diameter ( $d_m$ ), showing an increase in  $d_m$  with an increase in oxygen content in the ambient environment. These results demonstrate that overall NP agglomerates are larger at increased oxygen levels, similar to Al<sub>m</sub>O<sub>n</sub> clusters size observed by QCC mass spectrometry (Figure 4).

To further investigate NP agglomeration behavior, we examine the miniSPLAT-measured vacuum aerodynamic diameter ( $d_{va}$ ) size distributions presented in Figure 6(a). The figure

shows that in both N<sub>2</sub> and air environments the  $d_{va}$  distributions are bimodal, with the first narrow peaks at  $\approx 50$  nm and broad peaks at larger  $d_{va}$  sizes. The narrow peaks correspond to NP agglomerates with fractal morphologies with vacuum aerodynamic diameters that are nearly independent of their mass and mobility diameter ( $d_m$ ).<sup>35</sup> This phenomenon is illustrated in Figure 7(a), which shows the miniSPLAT-measured  $d_{va}$  size distributions of mobility-selected fractal NP agglomerates particles, generated in air. The simultaneous measurements of  $d_{va}$  and  $d_m$  for fractal NP agglomerates yield measurements of their effective density as a function of their  $d_m$  (Figure 7(b)). Results reported in Figure 7(b) showing  $d_m$ , with a slope that yields fractal dimension of  $D_{fa} \approx 2$ , indicative of fractal NP agglomerates. The values of effective densities are significantly lower than the material density of Al<sub>2</sub>O<sub>3</sub> (3.95 gcm<sup>-3</sup>), consistent with a small size of primary NP and large size-dependent void fraction of fractal NP agglomerates.

The second broad peaks in Figure 6(a) correspond to more compact NP agglomerates, which have a wide range of shapes

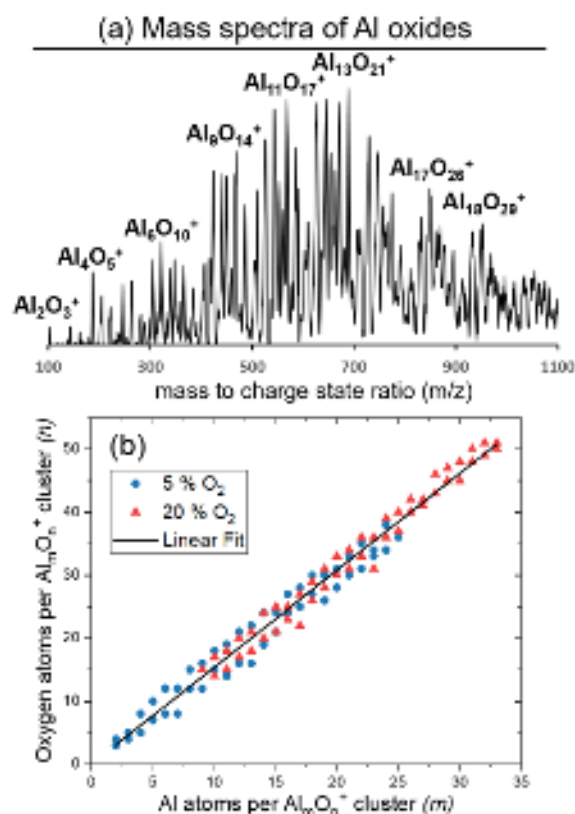


FIG. 4. (a) A mass spectrum showing the formation of  $Al_mO_n^+$  clusters in 5%  $O_2$ , balance  $N_2$ . (b) Plot illustrating the range of  $Al_mO_n^+$  clusters formed at 5% (blue circles) and 20% (red triangles)  $O_2$ . The linear fit ( $y = 1.54x + 0.02$ ,  $R^2=0.98$ ) indicates  $\approx 1.5$  O atoms are found per Al atom in both environments.

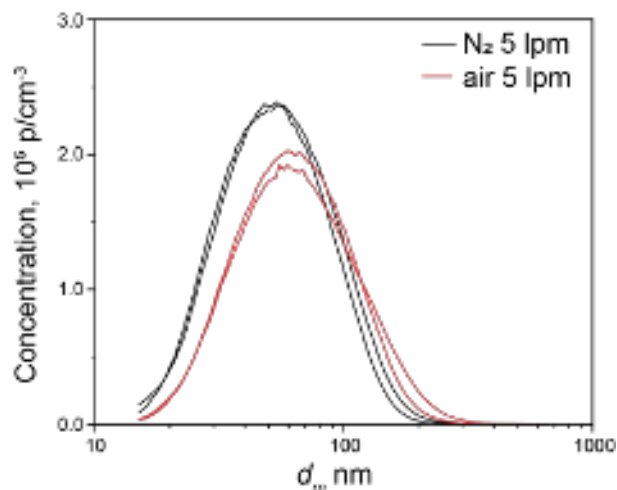


FIG. 5. SMPS-measured mobility diameter size distributions of particulates generated in nitrogen and air. The gas flow rate used was 5 lpm.

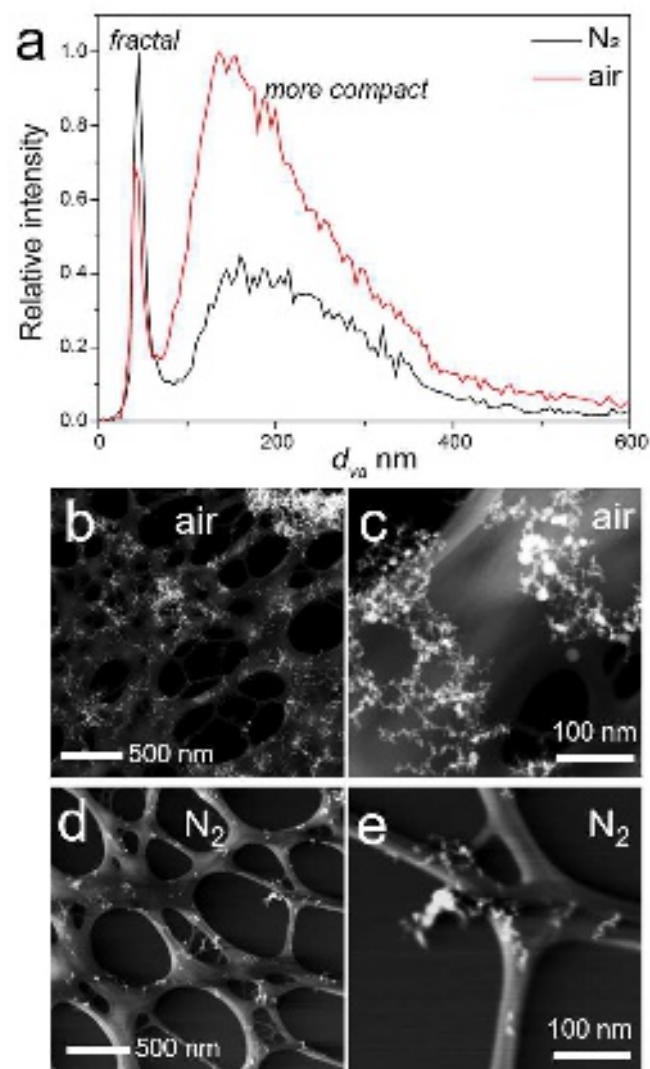


FIG. 6. (a) miniSPLAT-measured vacuum aerodynamic diameter size distributions of particulates generated in nitrogen and air. Note that for ease of comparison, each size distribution was normalized by the total particle number. (b-e) STEM imaging of NP agglomerates generated via laser ablation of AA6061 in the air (b,c) and in  $N_2$  (d,e) ambient gases.

and effective densities. In air, we find that more compact NP agglomerates represent higher number fraction of particulates as compared to  $N_2$  environment. We can easily visualize this difference in NP agglomerate morphology with the STEM images provided in Figure 6(b) - (e).

Mass spectra of NP agglomerates were collected using miniSPLAT and are reported in Figures 8 (a) and (b) for air and  $N_2$ , respectively. Both show the same prominent peaks (i.e., O, Al, AlO, AlO<sub>2</sub>, Al<sub>2</sub>O<sub>3</sub>), although with varying relative intensities for each environment. In air, the Al metal and monoxide peaks have similar intensities. However, in  $N_2$ , the relative intensity of the Al elemental peak is significantly higher than the AlO and other molecular peaks. Figure 8b shows the presence of Al oxide mass spectral peaks in the  $N_2$

This is the author's peer reviewed, accepted manuscript. However, the online version of record will be different from this version once it has been copyedited and typeset.

PLEASE CITE THIS ARTICLE AS DOI: 10.1063/5.0167400

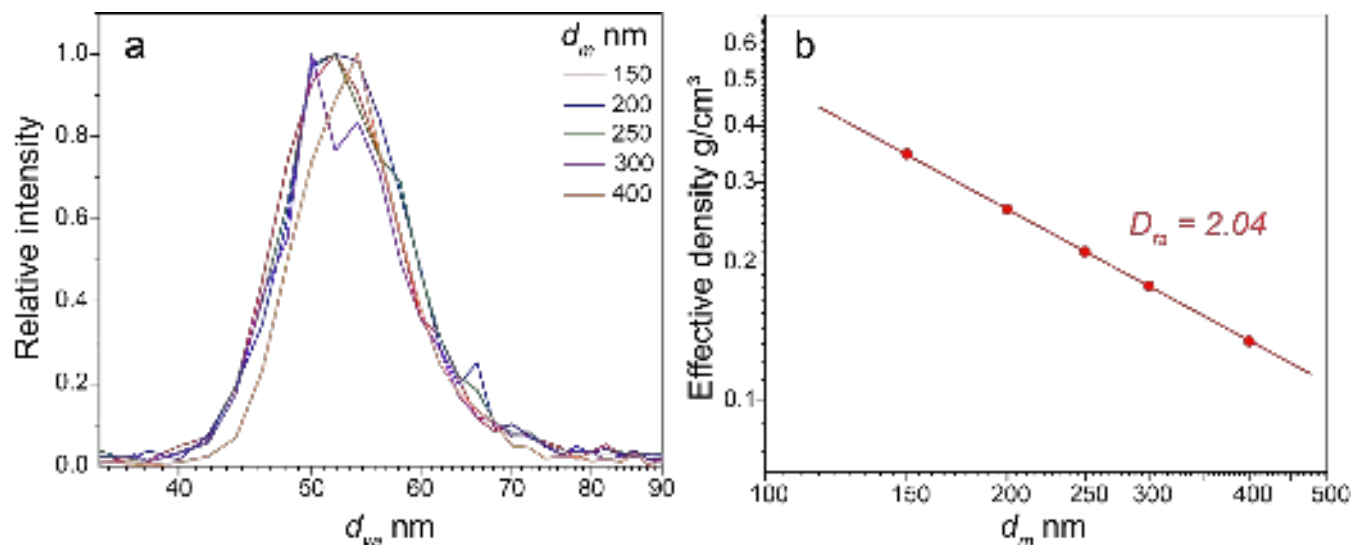


FIG. 7. (a) miniSPLAT-measured vacuum aerodynamic diameter size distributions of mobility-selected fractal NP agglomerates, generated in air. These measurements are used to calculate particle effective density as a function of their mobility diameter ( $d_m$ ). Note that for ease of comparison, all size distributions were normalized to the same maximum peak height; (b) Plot of the calculated effective density as a function of  $d_m$ , displayed in a log-log domain, showing power law relationship.

environment. This is due to the presence of trace  $O_2$ , which is unavoidable in the flow-through experimental setup used for particulate analysis. The presence of even trace  $O_2$  will lead to Al oxide formation.<sup>38</sup> AlN is detected in both air and flowing  $N_2$  environments.

Characterization via (S)TEM was performed for NPs generated in air and  $N_2$  environments, with results given in Figures 9 and 10, respectively. Darkfield images in Figure 9(a) and (b) show examples of NP agglomerates formed in air. Yellow and red arrows given in (a) and (b) indicate individual AlN and  $Al_2O_3$  NPs shown in HR-TEM images in (c) and (d), respectively. The HR-TEM data in (d) is indexed as  $Al_2O_3$  based on QCQ mass spectrometry results that show late time (100 - 500  $\mu s$ ) formation of  $Al_{2x}O_{3x}^+$  clusters which increase in size with increased oxygen availability. STEM-EDS of a region shown in (e) highlights NPs have a strong Al signal, some NPs have N signal whereas others have O signal, and there do appear to be regions where O and N signals are co-located. Based on the results reported in Figure 9, Al oxide and nitride NPs appear to have co-precipitated in LA plumes.

In  $N_2$ , similar fractal morphologies were observed as in the air environment, although with less agglomeration and more open/empty space, as seen in Figure 10(a)-(b). Similar to air, both oxide and nitride individual NPs were observed, noted in sub-figures (a)-(b). STEM-EDS mapping illustrates NP agglomerates contain Al, O, and N signals, where in some cases O and N signals are co-located, similar to the results shown for NPs formed in air (Figure 9). The co-location of O and N signals may be attributed to overlapping NPs imaged via STEM.

#### IV. DISCUSSION

In laser-generated plumes, the evolution from ions and atoms to molecules, clusters, NPs, and NP agglomerates begins at plasma onset (i.e., time zero) and occurs over nanosecond to millisecond timescales. By monitoring the evolution of LPP plume species, we can begin to reconstruct the processes that are expected to occur in an HE event, in which physical conditions may be similar to those in lab-scale surrogates. However, it must be emphasized that although the sequence of particulate formation routes may be similar in HE events and LA plumes, the initiation times and duration of these processes will differ significantly in addition to the differences in length scales. For example, an important difference between LPPs and HE events is that in HE events, the burning of metal fragments can lead to the introduction of Al species at a later time scale in comparison to in an LPP where all Al is vaporized via LA (at plasma onset).<sup>44</sup>

Several factors will influence the processes involved in NP formation and agglomeration, including plasma physical conditions and the thermo- and plasma-chemical reactions occurring in the LPP.<sup>4</sup> Given that LPPs are inherently heterogeneous in both space and time,<sup>36</sup> we also expect the thermo- and plasma-chemical reactions contributing to molecule, cluster, and NP formation to vary with respect to the spatial position in the LPP and the time after plasma onset.<sup>6,45</sup> The role of laser-plasma coupling (an important consideration in ns LPPs) will also lead to greater initial plasma temperatures than would be observed in fireballs. At early times, the presence of high plasma temperatures inhibits molecular formation in LA plumes. As time evolves, the temperature of the system decreases rapidly due to plasma expansion and collisions with the cold ambient environment. We noticed both ex-

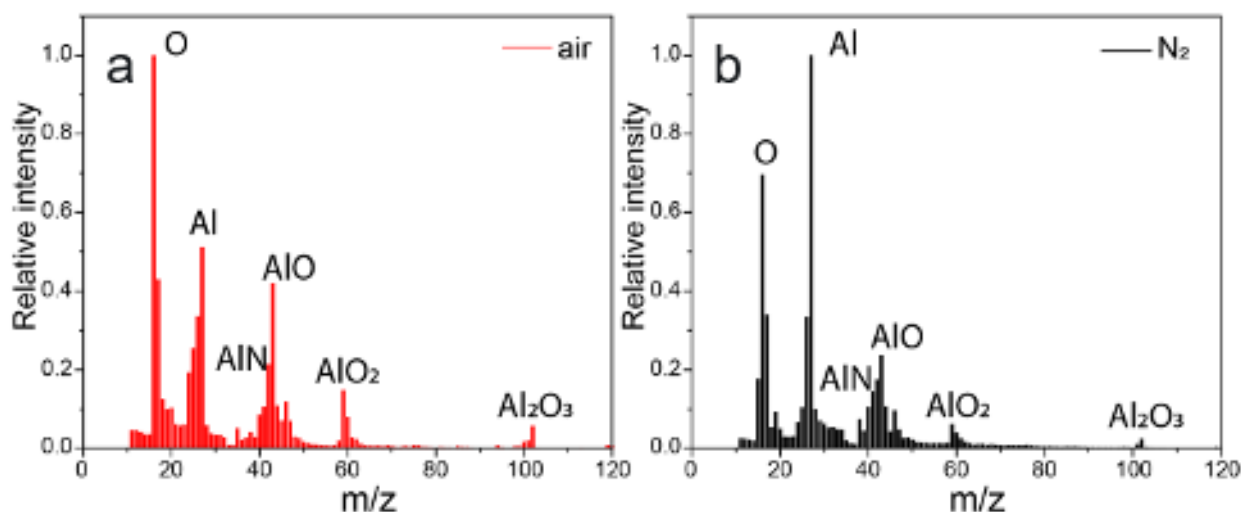


FIG. 8. Average negative ion mass spectra from miniSPLAT of all ionized agglomerate fragments generated in: (a) air, and (b) flowing  $N_2$ .

citation temperature and electron densities are similar at early times ( $\leq 3\mu s$ ) both in air and  $N_2$ , indicating that initial plasma physical conditions are not significantly impacted by the presence of  $O_2$  in the environment. This is not surprising considering the confinement properties of both air and  $N_2$  gases are somewhat similar.<sup>46</sup> The temperature measurement in the air ambient showed a discontinuity between the excitation temperature measured from Al ions and AIO molecules. This may be correlated to the inhomogeneity of species distribution in the plasma.<sup>36</sup> The ions and atoms primarily exist in the hotter regions of the plasma while molecules are formed in the cooler regions.<sup>45</sup> At times  $\geq 5\mu s$  we were not able to reliably determine the temperature in plasmas generated in  $N_2$  due to relatively weak AlN emission.

Molecular formation is favored when the temperatures of the system become  $\leq 8000$  K,<sup>4,47</sup> and ions and atoms are consumed in the formation of smaller molecules such as diatoms (e.g.,  $Al + O_2 \leftrightarrow AIO + O$ ). In both air and  $N_2$ , we expect similar plume confinement, and hence similar plasma hydrodynamic processes can occur,<sup>46</sup> although chemical reactions in both environments will occur at different times during the LPP lifecycle. Prior work has highlighted that molecular formation occurs preferentially at the cooler plume periphery.<sup>9,45,48</sup> We similarly expect that cluster formation and nucleation of NPs may occur heterogeneously, leading to a distribution of cluster sizes, and NPs with varying sizes, compositions, and crystal structures.<sup>6</sup> Previous studies also reported that the presence of  $O_2$  in the ambient gas affects the persistence of atomic species in the plume as well as the plume temperature decay.<sup>47</sup> In this study we find that  $O_2$  availability in the environment also significantly impacts the species produced in LPPs, their temporal evolution, cluster size, NP and agglomerate size distribution, and average composition. In particular, we observe stronger atomic emission (Al I) in  $N_2$  in comparison to air, which is consistent with mass spectra measured via miniSPLAT (Figure 8) that also shows the Al elemental peak has a higher relative intensity in  $N_2$  than

in air. In the air, AIO formation is prominent during times 10-100  $\mu s$  and no strong AlN signal is observed. However, since AlN NPs were identified via STEM, it is likely AlN molecules are present in LPPs. The strong emission of AIO over AlN could be due to the longer radiative lifetimes of AIO compared to AlN.<sup>42,49</sup> The relatively weak AlN signal could also be related to differences in thermo-chemistry of AIO and AlN formation, which will lead to a significantly lower number density of AlN compared to AIO molecules. This suggestion is also supported by the average agglomerate particle mass spectra (obtained using miniSPLAT, Figure 8) that show similar species are present in both air and  $N_2$  environments (including AIO,  $Al_2O_3$ ,  $AIO_2$ , AlN), but with different relative intensities.

AlN is not observed using QCQ mass spectrometry in  $N_2$ . At later times in plasma evolution (100 - 500  $\mu s$ ), Al oxide clusters are formed with an approximate stoichiometry of  $Al_2O_3$ . When  $O_2$  availability is increased, this ratio remains constant, although cluster size increases. From the combination of optical spectroscopy and QCQ mass spectrometry, we can hypothesize that the evolution of species in LPPs progresses from ions and atoms to oxide molecules (such as AIO), which are then consumed in the formation of higher oxides (e.g.,  $AIO_2$ ,  $Al_2O_2$ , etc.) and  $Al_2O_3$  clusters. These clusters then act as nucleation sites for oxide NPs. This formation of AIO molecules and Al oxide clusters and NPs occurs when  $O_2$  is present (even if only in trace amounts). These results are consistent with particle mass spectrometry and STEM results, where we find that oxides are formed even with only trace  $O_2$  present in the ambient, but may exist in lower number densities in LPPs, making them difficult to probe via OES.

All characterized particles were NP agglomerates, although with different size distributions depending on  $O_2$  availability; NP size distributions are shifted to greater  $d_m$  values in air versus  $N_2$ . Greater  $O_2$  availability may lead to supersaturation of the vapor phase with AIO or other low order Al oxide molecules that can act as nucleation sites for  $Al_mO_n$  NPs. A

This is the author's peer reviewed, accepted manuscript. However, the online version of record will be different from this version once it has been copyedited and typeset.

PLEASE CITE THIS ARTICLE AS DOI: 10.1063/5.0167400

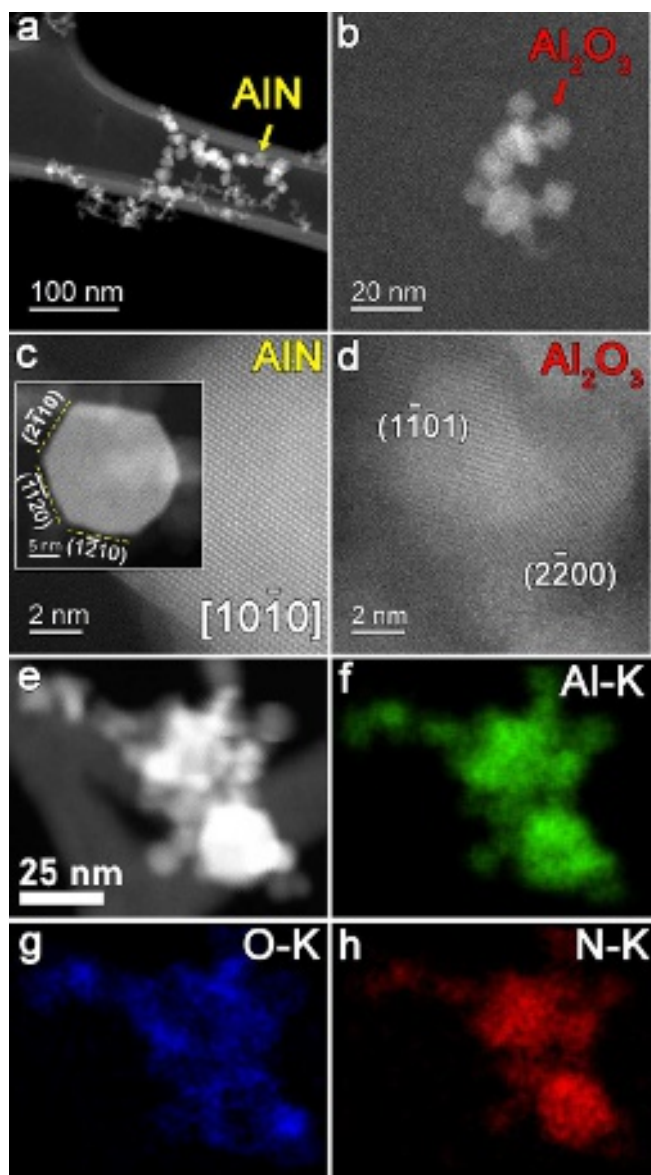


FIG. 9. Ambient air LPP particles: (a, b) Dark Field (DF)-TEM images of NPs with fractal morphology. Arrows in (a) and (b) indicate AlN and  $\text{Al}_2\text{O}_3$  NPs, respectively. (c, d) HR-TEM images of AlN and  $\text{Al}_2\text{O}_3$  NPs, (e) STEM image of NPs, and (f, g, h) STEM-EDS maps for Al, O, and N, respectively.

greater density of oxide nucleation sites could lead to a greater number of nucleated NPs that grow and impinge upon each other, which could contribute to greater agglomeration in air.

A schematic summarizing evolution of plasma species in air and  $\text{N}_2$  (with trace  $\text{O}_2$ ) environments is provided in Figure 11. This schematic highlights that species present in plasmas expanding into air and  $\text{N}_2$  environments are similar, although a higher density of oxide species is present in air. In addition, the extent of agglomeration is greater in air when compared to  $\text{N}_2$ , which is a key finding from this study.

## V. CONCLUSIONS

The impact of oxygen availability in the environment on molecular, cluster, and NP formation and NP agglomeration was studied using LA plumes in air and  $\text{N}_2$  ambient gases. Multiple complementary *in-situ* and *ex-situ* experimental techniques were used to capture processes occurring over a wide range of time and length scales. Namely, OES, QCQ mass spectrometry, miniSPLAT, and STEM were used to track the kinetics of molecular formation, cluster size and stoichiometry, NP properties, mass spectra of NP agglomerates, and individual NP crystal structure and element distributions.

Our results highlight that initial plasma physical conditions are similar in air and  $\text{N}_2$  environments, although species dominant in the plume vary at later times. Spectral features in the air are dominated by Al neutral atoms and AlO molecules, whereas in  $\text{N}_2$ , Al atoms and AlN are dominant. Using QCQ mass spectrometry we find that increasing  $\text{O}_2$  in the environment leads to the formation of larger Al oxide clusters between 100 - 500  $\mu\text{s}$  after plasma onset, with an approximate stoichiometry of  $\text{Al}_2\text{O}_3$ , and more compact NP agglomerates are found using miniSPLAT and *ex-situ* techniques. Individual NPs are found to be either  $\text{Al}_2\text{O}_3$  or AlN. Both oxide and nitride NPs are found in air and  $\text{N}_2$  environments, indicating that only trace  $\text{O}_2$  is needed to form  $\text{Al}_2\text{O}_3$ . The approach utilized here and the reported findings have implications for elucidating mechanisms of debris formation in HE-type events, in which Al or Al alloys may be present.

The present work highlights that the presence of  $\text{O}_2$  in the ambient gas significantly impacts spectral signatures, cluster size, and NP agglomeration behavior; all relevant to understanding debris formation. Further work incorporating hydrodynamic and plasma chemistry modeling could help inform how  $\text{O}_2$  in the ambient environment can lead to increased NP agglomerate size. In addition, the fate of minor alloying elements in NP formation requires further study. Here, minor alloying elements including Cu, Zn, and Fe were detected in miniSPLAT positive ion mass spectra, however, the location of these elements in NPs was not clear from STEM data, likely due to their low concentrations. Microscopy techniques that are more sensitive to the composition may help explain the distribution and concentration of such minor alloying elements,<sup>50</sup> which may inform forensic investigations.

## ACKNOWLEDGMENTS

This work was supported by the DOE/NNSA Office of Defense Nuclear Nonproliferation Research and Development (DNN R&D) and by the Department of the Defense, Defense Threat Reduction Agency (DTRA) under award number HDTRA1-20-2-0001. The content of the information does not necessarily reflect the position or the policy of the federal government, and no official endorsement should be inferred. Pacific Northwest National Laboratory is a multi-program national laboratory operated by Battelle for the U.S. Department of Energy under Contract DE-AC05-76RL01830.

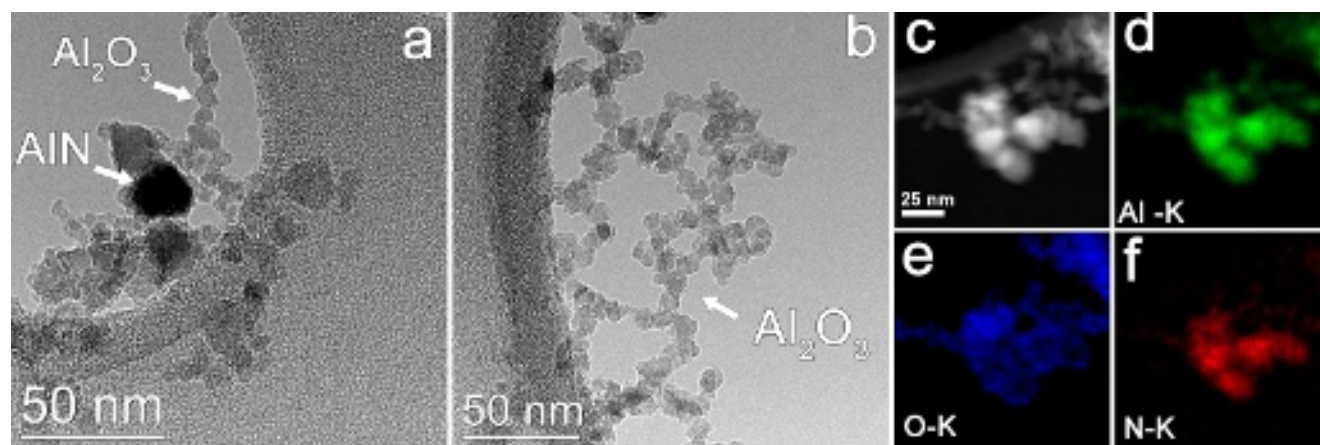


FIG. 10. TEM results show the fractals consisting of  $\text{Al}_2\text{O}_3$  and AlN NPs formed following LA in nitrogen and entrained in flowing  $\text{N}_2$  with trace  $\text{O}_2$ . (a-b) BF-TEM images where the  $\text{Al}_2\text{O}_3$  and AlN particles are highlighted by white arrows. (c) STEM image of NPs, and (d, e, f) STEM-EDS results show the distribution of Al, O, and N, respectively.



FIG. 11. Schematic summarizing the evolution of plasma species in laser ablation plumes to NP and NP agglomerate formation for air and  $\text{N}_2$  (with trace  $\text{O}_2$ ) environments.

#### DATA AVAILABILITY STATEMENT

The data that support the findings of this study are available upon reasonable request from the corresponding author.

#### REFERENCES

- <sup>1</sup> *Military Handbook: Metallic Materials and Elements for Aerospace Vehicle Structures*, Vol. 1 (US Department of Defense, 1990).
- <sup>2</sup> K. P. Brooks and M. W. Beckstead, "Dynamics of aluminum combustion," *J. Propuls. Power.* **11**, 769–780 (1995).
- <sup>3</sup> C. Rossi, K. Zhang, D. Esteve, P. Alphonse, P. Tailhades, and C. Vahlas, "Nanoenergetic materials for mems: a review," *J. Microelectromech. Syst.* **16**, 919–931 (2007).
- <sup>4</sup> E. J. Kautz, E. N. Weerakkody, M. S. Finko, D. Curreli, B. Koroglu, T. P. Rose, D. G. Weisz, J. C. Crowhurst, H. B. Radousky, M. DeMagistris, *et al.*, "Optical spectroscopy and modeling of uranium gas-phase oxidation: Progress and perspectives," *Spectrochim. Acta B* **75**, 106283 (2021).
- <sup>5</sup> S. S. Harilal, B. E. Brumfield, and M. C. Phillips, "Lifecycle of laser-produced air sparks," *Phys. Plasmas* **22**, 063301 (2015).
- <sup>6</sup> E. J. Kautz, A. Zelenyuk, B. Gwalani, M. C. Phillips, and S. S. Harilal, "Gas-phase oxidation and nanoparticle formation in multi-element laser ablation plumes," *Phys. Chem. Chem. Phys.* **24**, 26583–26590 (2022).
- <sup>7</sup> E. R. Wainwright, S. W. Dean, F. C. De Lucia, T. P. Weihs, and J. L. Gottfried, "Effect of sample morphology on the spectral and spatiotemporal characteristics of laser-induced plasmas from aluminum," *Appl. Phys. A* **126**, 1–18 (2020).
- <sup>8</sup> E. H. Kwapis, J. W. Posey, E. Medici, K. Berg, R. W. Houim, and K. C. Hartig, "Experimental and computational investigation into the hydrodynamics and chemical dynamics of laser ablation aluminum plasmas," *Phys. Chem. Chem. Phys.* **25**, 15666–15675 (2023).
- <sup>9</sup> S. S. Harilal, B. E. Brumfield, B. D. Cannon, and M. C. Phillips, "Shock wave mediated plume chemistry for molecular formation in laser ablation plasmas," *Anal. Chem.* **88**, 2296–2302 (2016).
- <sup>10</sup> C. Kimblin, R. Trainham, G. A. Capelle, X. Mao, and R. E. Russo, "Characterization of laser-induced plasmas as a complement to high-explosive large-scale detonations," *AIP Adv.* **7**, 095208 (2017).
- <sup>11</sup> K. R. Campbell, N. R. Wozniak, J. P. Colgan, E. J. Judge, J. E. Barefield, D. P. Kilcrease, M. P. Wilkerson, K. R. Czerwinski, and S. M. Clegg, "Phase discrimination of uranium oxides using laser-induced breakdown

- spectroscopy," *Spectrochim. Acta B* **134**, 91–97 (2017).
- <sup>12</sup>M. Liezers, A. J. Fahey, A. J. Carman, and G. C. Eiden, "The formation of trinitite-like surrogate nuclear explosion debris (sned) and extreme thermal fractionation of SRM-612 glass induced by high power cw CO<sub>2</sub> laser irradiation," *J. Radioanal. Nucl. Chem.* **304**, 705–715 (2015).
- <sup>13</sup>S. R. Taylor and M. D. Denny, "An analysis of spectral differences between Nevada test site and Shagan River nuclear explosions," *J. Geophys.* **96**, 6237–6245 (1991).
- <sup>14</sup>M. C. Phillips, S. S. Harilal, J. Yeak, R. Jason Jones, S. Wharton, and B. E. Bernacki, "Standoff detection of chemical plumes from high explosive open detonations using a swept-wavelength external cavity quantum cascade laser," *J. Appl. Phys.* **128**, 163103 (2020).
- <sup>15</sup>W. Lewis, C. Rumchik, and M. Smith, "Emission spectroscopy of the interior of optically dense post-detonation fireballs," *J. Appl. Phys.* **113**, 024903 (2013).
- <sup>16</sup>E. N. Weerakkody, B. A. Read, M. D. Clemenson, N. G. Glumac, *et al.*, "Uranium dust cloud combustion: Burning characteristics and absorption spectroscopy measurements," *J. Combust.* **2022**, 3570238 (2022).
- <sup>17</sup>A. Butler, D. Amondson, H. Krier, and N. Glumac, "Spectral emission signatures from cased high explosive charges," *Appl. Spectrosc.* **75**, 1410–1418 (2021).
- <sup>18</sup>R. Lodes, H. Krier, and N. Glumac, "Spectrally- and temporally-resolved optical depth measurements in high explosive post-detonation fireballs," *Propellants, Explosives, Pyrotechnics* **45**, 406–415 (2020).
- <sup>19</sup>M. D. Straub, J. Arnold, J. Fessenden, and J. L. Kiplinger, "Recent advances in nuclear forensic chemistry," *Anal. Chem.* **93**, 3–22 (2020).
- <sup>20</sup>M. S. Finko, D. Curreli, D. G. Weisz, J. C. Crowhurst, T. P. Rose, B. Koroglu, H. B. Radousky, and M. R. Armstrong, "A model of early formation of uranium molecular oxides in laser-ablated plasmas," *J. Phys. D: Appl. Phys.* **50**, 485201 (2017).
- <sup>21</sup>L. Catoire, J.-F. Legendre, and M. Giraud, "Kinetic model for aluminum-sensitized ram accelerator combustion," *J. Propuls. Power.* **19**, 196–202 (2003).
- <sup>22</sup>A. Miller, G. Ahlstrand, D. Kittelson, and M. Zachariah, "The fate of metal (Fe) during diesel combustion: Morphology, chemistry, and formation pathways of nanoparticles," *Combustion and Flame* **149**, 129–143 (2007).
- <sup>23</sup>I. S. Altman, I. E. Agranovski, and M. Choi, "Mechanism of nanoparticle agglomeration during the combustion synthesis," *Appl. Phys. Lett.* **87**, 053104 (2005).
- <sup>24</sup>T. E. Itina, "On nanoparticle formation by laser ablation in liquids," *The J. Phys. Chem. C* **115**, 5044–5048 (2011).
- <sup>25</sup>E. Fazio, B. Gökce, A. De Giacomo, M. Meneghetti, G. Compagnini, M. Tommasini, F. Waag, A. Lucotti, C. G. Zanchi, P. M. Ossi, *et al.*, "Nanoparticles engineering by pulsed laser ablation in liquids: concepts and applications," *Nanomaterials* **10**, 2317 (2020).
- <sup>26</sup>S. Noël, J. Hermann, and T. Itina, "Investigation of nanoparticle generation during femtosecond laser ablation of metals," *Applied Surface Science* **253**, 6310–6315 (2007).
- <sup>27</sup>M. Kim, S. Osone, T. Kim, H. Higashi, and T. Seto, "Synthesis of nanoparticles by laser ablation: A review," *KONA Powder and Particle Journal* **34**, 80–90 (2017).
- <sup>28</sup>A. B. Hartanto, X. Ning, Y. Nakata, and T. Okada, "Growth mechanism of ZnO nanorods from nanoparticles formed in a laser ablation plume," *Appl. Phys. A* **78**, 299–301 (2004).
- <sup>29</sup>E. J. Kautz, M. C. Phillips, and S. S. Harilal, "Tantalum oxide and nitride spectral features from a laser-produced plasma," *Spectrochim. Acta B* **203**, 106659 (2023).
- <sup>30</sup>ASTM B209, "Standard specification for aluminum and aluminum-alloy sheet and plate," Standard (ASTM International, West Conshohocken, PA, 2022).
- <sup>31</sup>M. J. Manard, P. R. Kemper, R. Trainham, and P. Armentrout, "Sigma bond activation of deuterium mediated by atomic cerium cations: Experiment and theory," *Int. J. Mass Spectrom.* **441**, 19–24 (2019).
- <sup>32</sup>P. R. Kemper and M. T. Bowers, "A hybrid double-focusing mass spectrometer—high-pressure drift reaction cell to study thermal energy reactions of mass-selected ions," *J. Am. Soc. Mass Spectrom.* **1**, 197–207 (1990).
- <sup>33</sup>P. R. Kemper, P. Weis, and M. T. Bowers, "Cr+ (h2) n clusters: Asymmetric bonding from a symmetric ion," *Int. J. Mass Spectrom.* **160**, 17–37 (1997).
- <sup>34</sup>A. Zelenyuk, D. Imre, J. Wilson, Z. Zhang, J. Wang, and K. Mueller, "Airborne single particle mass spectrometers (SPLAT II & miniSPLAT) and new software for data visualization and analysis in a geo-spatial context," *J. Am. Soc. Mass Spectrom.* **26**, 257–270 (2015).
- <sup>35</sup>K. J. Suski, D. M. Bell, M. K. Newburn, M. L. Alexander, D. Imre, D. W. Koppenaal, and A. Zelenyuk, "Real-time characterization of particles produced by laser ablation for analysis by inductively coupled plasma mass spectrometry," *Spectrochim. Acta B* **179**, 106092 (2021).
- <sup>36</sup>S. S. Harilal, M. C. Phillips, D. H. Froula, K. K. Anoop, R. C. Issac, and F. N. Beg, "Optical diagnostics of laser-produced plasmas," *Rev. Mod. Phys.* **94**, 035002 (2022).
- <sup>37</sup>C. M. Western, "PGOPHER: A program for simulating rotational, vibrational and electronic spectra," *J. Quant. Spectrosc. Rad. Transf.* **186**, 221–242 (2017).
- <sup>38</sup>E. J. Kautz, M. C. Phillips, A. Zelenyuk, and S. S. Harilal, "Oxidation in laser-generated metal plumes," *Phys. Plasmas* **29**, 053509 (2022).
- <sup>39</sup>R. L. Kurucz, "The Kurucz Smithsonian atomic and molecular database," in *Astrophysical Applications of Powerful New Databases*, Vol. 78 (1995) p. 205.
- <sup>40</sup>N. Konjević and W. Wiese, "Experimental Stark widths and shifts for spectral lines of neutral and ionized atoms," *J. Phys. Chem. Ref. Data* **19**, 1307–1385 (1990).
- <sup>41</sup>N. Glumac, "Aluminum nitride emission from a laser-induced plasma in a dispersed aerosol," *J. Appl. Phys.* **98**, 053301 (2005).
- <sup>42</sup>S. Johnson, G. Capelle, and H. Broida, "Laser excited fluorescence and radiative lifetimes of AlO (B 2Σ+– X 2Σ+)," *The Journal of Chemical Physics* **56**, 663–665 (1972).
- <sup>43</sup>L. Catoire, J.-F. Legendre, and M. Giraud, "Kinetic model for aluminum-sensitized ram accelerator combustion," *J. Propuls. Power.* **19**, 196–202 (2003).
- <sup>44</sup>P. Lynch, G. Fiore, H. Krier, and N. Glumac, "Gas-phase reaction in nanoaluminum combustion," *Combustion science and technology* **182**, 842–857 (2010).
- <sup>45</sup>E. J. Kautz, P. J. Skrodzki, M. Burger, B. E. Bernacki, I. Jovanovic, M. C. Phillips, and S. S. Harilal, "Time-resolved imaging of atoms and molecules in laser-produced uranium plasmas," *J. Anal. At. Spectrom.* **34**, 2236–2243 (2019).
- <sup>46</sup>P. J. Skrodzki, M. Burger, I. Jovanovic, M. C. Phillips, B. E. Brumfield, J. Yeak, and S. S. Harilal, "Plume dynamics and gas-phase molecular formation in transient laser-produced uranium plasmas," *Phys. Plasmas* **26**, 083508 (2019).
- <sup>47</sup>S. S. Harilal, E. J. Kautz, B. E. Bernacki, M. C. Phillips, P. Skrodzki, M. Burger, and I. Jovanovic, "The physical conditions for UO formation in laser-produced uranium plumes," *Phys. Chem. Chem. Phys.* **21**, 16161 (2019).
- <sup>48</sup>E. R. Wainwright, F. De Lucia, T. P. Weihs, and J. L. Gottfried, "Spatiotemporal and emission characteristics of laser-induced plasmas from aluminum-zirconium composite powders," *Spectrochim. Acta B* **183**, 106270 (2021).
- <sup>49</sup>W. Xing, D. Shi, J. Sun, and Z. Zhu, "Radiative lifetimes of vibrational levels and transition probabilities of spontaneous emissions of the six lowest-lying triplet states of AlN radical," *Spectrochim. Acta A* **217**, 77–85 (2019).
- <sup>50</sup>E. J. Kautz, S. V. Lambeets, J. Royer, D. E. Perea, S. S. Harilal, and A. Devaraj, "Compositional partitioning during early stages of oxidation of a uranium-molybdenum alloy," *Scripta Materialia* **212**, 114528 (2022).